PCCP

PAPER

View Article Online
View Journal | View Issue

Cite this: *Phys. Chem. Chem. Phys.*, 2016, **18**, 12350

First-principles study of line-defect-embedded zigzag graphene nanoribbons: electronic and magnetic properties†

Zhaoyong Guan,*[a] Chen Si,[b] Shuanglin Hu[c] and Wenhui Duan[ad]

Received 24th February 2016,
Accepted 31st March 2016

DOI: 10.1039/c6cp01263a

www.rsc.org/pccp

Based on first-principles calculations, we present the electronic and magnetic properties of a class of line defect-embedded zigzag graphene nanoribbons, with one edge saturated by two hydrogen atoms per carbon atom and the other edge terminated by only one hydrogen atom. Such edge-modified nanoribbons without line defects are found to be typical bipolar magnetic semiconductors (BMS). In contrast, when the line defect is introduced into the ribbons, the ground state is ferromagnetic, and the resulting nanoribbons can be tuned to spin-polarized metal, metal with Dirac point, or half-metal by varying the position of the line defect, owing to the defect-induced self-doping of the BMS. Specifically, when the line defect is far away from the edges of the ribbon, the system shows half-metallicity. We further confirm the structural and magnetic stability at room temperature by first-principles molecular dynamics simulations. Our findings reveal the possibility of building metal-free electronic/spintronic devices with magnetic/half-metallic graphene nanoribbons.

1. Introduction

Graphene nanoribbons (GNRs), which are quasi-1D graphene nanostructures, have attracted considerable attention due to their fascinating electronic and magnetic properties.[1–7] Depending on the different orientations along which graphene is cut, GNRs can show different edge types, among which the zigzag and armchair edges are the most common types experimentally. Several experimental and theoretical studies have shown that the edge types of graphene nanoribbons strongly influence their electronic and magnetic properties.[2,3,5–7] The armchair edge graphene nanoribbons (AGNRs) are found to be non-magnetic semiconductors with band gaps oscillating with the widths.[2,7] The zigzag edge graphene nanoribbons (ZGNRs) exhibit semiconductor ground state with two electronic edge states, which are ferromagnetically ordered in each edge but antiferromagnetically coupled with each other.[3] The ZGNRs show interesting transport and magnetic properties.[6,8–12] Moreover, the ZGNR can be further converted into a half metal under a very strong in-plane electric field, which paves the way to exploring metal-free spintronics at the nanometer scale based on graphene-based materials.[1,11,13–18]

The controlled modification of the two ZGNR edges with different functional groups suggests a natural way to build the in-plane electric field and offers more options to devise and adjust the magnetic properties of ZGNRs. For example, when a ZGNR is terminated by NO_2 groups at one edge and CH_3 groups on the other side, antiferromagnetic half-metallicity can be observed without the presence of an external electric field.[13] Interestingly, it was predicted that the antiferromagnetic ZGNR can be changed into a ferromagnetic semiconductor when one edge is passivated by one hydrogen per edge carbon atom (modified to C–H, sp^2-bonded hybrid bonding) and the other is saturated by two hydrogens per edge carbon atom (modified to C–2H, sp^3-bonded hybrid bonding).[16,17] Meanwhile, introducing defects is an alternative way to modify the properties of ZNGRs. It has been reported that different kinds of defects, such as point vacancies,[21] and line-defects (LD),[22–26] grain boundaries, *etc.* would affect the magnetic properties. Yazyev *et al.* found that each single vacancy defect of graphene contributes a magnetic moment of about 1.0 μ_B.[19,20] Okada *et al.* found that line defects introduce ferromagnetic spin ordering into the carbon nanotubes.[22] Kou *et al.* showed that strain tunes the magnetism of graphene sheets *via* line defect because of the charge redistribution around the line defect.[23] However, to our best knowledge, the synergy effects of edge modification and interior line defects

[a] *Department of Physics and State Key Laboratory of Low-Dimensional Quantum Physics, Tsinghua University, Beijing 100084, P. R. China. E-mail: zyguan@tsinghua.edu.cn; Fax: +86-010-62790614; Tel: +86-010-62790614*
[b] *School of Materials Science and Engineering, Beihang University, Beijing 100191, P. R. China*
[c] *Institute of Nuclear Physics and Chemistry, China Academy of Engineering Physics, Mianyang, Sichuan 621900, P. R. China*
[d] *Collaborative Innovation Center of Quantum Matter, Tsinghua University, Beijing 100084, P. R. China*

† Electronic supplementary information (ESI) available. See DOI: 10.1039/c6cp01263a

on the electronic and magnetic properties of GNRs have not been clearly shown. It was previously found that normal ZGNRs with one-dimensional topological line defects consisting of a pair of pentagons and one octagon (5-8-5) are antiferromagnetic semiconductors,[24–26] which inhibits their further application in nanoelectronics. While ZGNRs with one edge modified with C–H and the other edge with C–2H show ferromagnetic ground state,[27] it is natural to ask what would happen if the 5-8-5 line defect is embedded into those ZGNRs. In this work, we thus introduce the line defect into the ZGNRs with hetero-modification, corresponding to one edge modified to C–H and the other edge to C–2H, to study the combined impacts of line defects and edge modifications on the energetic, electronic and magnetic properties of ZGNRs.

2. Computational methods

In this study, our first-principles calculations are based on the density functional theory (DFT). The calculations of total energy and electronic properties are performed using the Vienna *ab initio* simulation package (VASP).[28,29] The projector-augmented wave (PAW) method is used to describe ion-electron interaction.[30,31] The Perdew–Burke–Ernzerhof (PBE) functional[32] with spin-polarized gradient correction and the screened hybrid functional Heyd–Scuseria–Ernzerhof (HSE06)[33] are adopted to describe the exchange and correlation interaction. The cutoff energy for the plane wave basis set is 500 eV, and the convergence threshold for total energy is 10^{-5} eV per super cell. For the Brillouin zone integration sampling, $1 \times 15 \times 1$, $1 \times 30 \times 1$, and $1 \times 60 \times 1$ *k*-point grids are used for geometry optimization, total energy, and density of states calculations, respectively. Geometry optimization without restricting symmetry is performed by using the conjugate gradient scheme[29] until the force acting on every atom is less than 10 meV Å^{-1}. The periodic boundary condition is set with the vacuum region in the dimension normal to the ribbon plane and with edges larger than 15 Å in order to avoid the effects of the virtually repeated neighboring images. *Ab initio* molecular dynamics (AIMD) simulations are also performed in the DFT framework. The constant moles–volume–temperature (*NVT*) ensemble[34] is adopted at room temperature (300 K), and the Nosé–Hoover thermostat is adopted.[35] The time step is set to 1 fs, and the total simulation time is 10 ps.

3. Results and discussion

3.1 The electronic and magnetic properties of H-*N*-2H: a new kind of BMS

To describe the ZGNRs in a well-defined way, we employ the customary notation (*i.e.*, A-ZGNR *N*-B) for the nanoribbons with different widths and edge modifications, where *N* represents the number of carbon zigzag chains, and A and B correspond to the termination atoms at the two ribbon edges, as shown in Fig. 1. For example, if one edge is saturated with one hydrogen atom per carbon (H) while the other edge is terminated with two hydrogen atoms per carbon (2H) to form a sp^3 type topology, the resulting

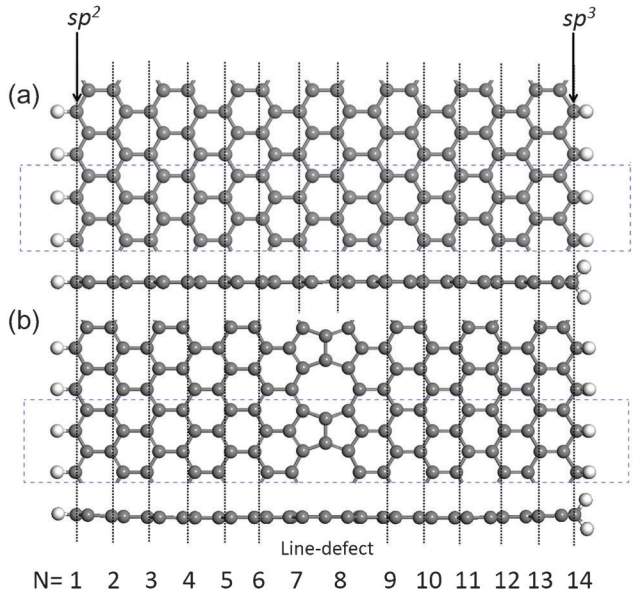

Fig. 1 Top view and side view of the optimized geometries of unit cells of (a) H-14-2H (C atoms of the left edge are in sp^2 hybridization, while those at the right edge are in sp^3 hybridization), (b) H-6-LD-6-2H ZGNR. The figures labeled with dashed lines show the perfect C chains. The gray and white balls stand for C and H atoms, respectively. The dashed rectangles in (a) and (b) indicate the cell used in calculations.

nanoribbons are denoted as H-ZGNR-2H. Fig. 1(a) shows the structure of H-ZGNR-2H with $N = 14$ (denoted "H-14-2H").

We first examine the geometries. As shown in Fig. 1(a), each carbon atom at the right edge of H-ZGNR-2H is saturated by two hydrogen atoms, forming sp^3 hybridization. The distance between the edge sp^3-hybridized C and its neighboring C atom is 1.52 Å, which is quite close to the length of the C–C bond in H_3C–CH_3 and diamond (1.54 Å). We also investigate the magnetic properties, finding that ferromagnetic (FM) configuration is the lowest-energy state, with a total magnetic moment of 2.00 μ_B (much larger than 0.80 μ_B in H-14-H) and spin density shown in Fig. 2.

The band structures of the FM state calculated with PBE and HSE06 functionals are shown in Fig. 2(a) and (b), respectively. It can be seen that H-14-2H is a semiconductor with an indirect band gap of 0.23 eV (with PBE functional). Most interestingly, we find that H-ZGNR-2H ($N = 14$) is a typical bipolar magnetic semiconductor (BMS) material,[37–39] with the valence and the conduction bands possessing opposite spin. When a gate voltage is applied or electrons/holes are doped into BMS materials, completely spin-polarized currents with reversible polarization can be created.[38–41] As schemed in Fig. 2(a), three energy parameters ($\Delta 1$, $\Delta 2$, and $\Delta 3$) are defined to characterize the BMS: $\Delta 1$ represents the spin–flip gap between the valence band maximum (VBM) and conduction band minimum (CBM), while $\Delta 1 + \Delta 2$ and $\Delta 1 + \Delta 3$ represent the spin-conserved gaps for the two spin channels, respectively. For H-14-2H, $\Delta 1$, $\Delta 2$ and $\Delta 3$ are 0.23, 0.36 and 0.40 eV, respectively. It is noted that the values of $\Delta 2$ and $\Delta 3$ are larger than that of $\Delta 1$. In this case, the stable half-metallicity could be achieved by electrical field or

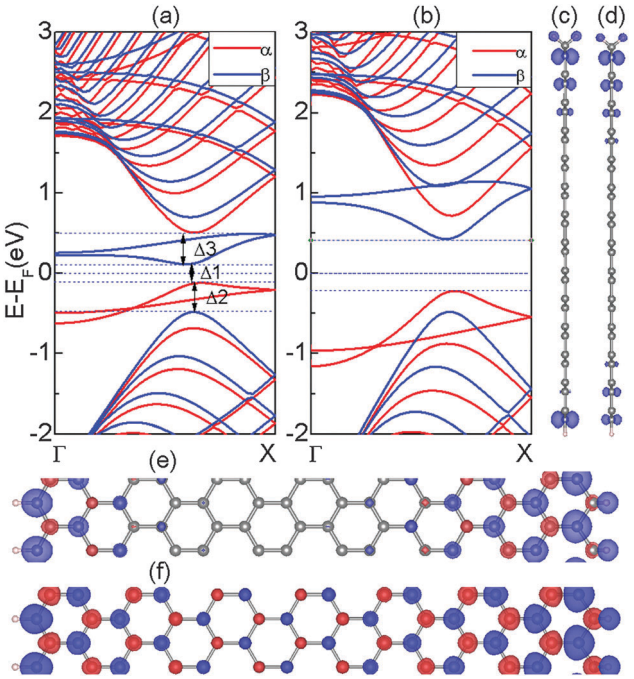

Fig. 2 Spin-polarized band structures calculated by using (a) PBE and (b) HSE06 functionals. The red and blue lines represent the band structures for the α-spin and β-spin, respectively. The Fermi level is set zero. The distribution of the charge density of the (c) VBM and (d) CBM of the FM ground state of H-14-2H calculated using the PBE functional. The spin density of H-14-2H with the FM ground state calculated by using (e) PBE and (f) HSE06 functionals. The blue and red represent α-spin and β-spin, respectively. The isovalue is set 0.06 e Å^{-3}.

chemical functionalization.[1,11,13] Fig. 2(c) and (d) show the charge densities of the VBM and CBM of the H-14-2H ZGNR, respectively. The VBM and CBM are mainly localized at the C atoms of the left sp^2 edge and the next-to-edge C atoms of the sp^3 edge, which resembles H-ZGNRs-H with strongly localized electron density, also at their sp^2 hybrid edges.[36]

However, given that the PBE functional could not exactly describe the system with strongly localized electrons due to underestimation of the effect of exchange correlation, it is expected that some more advanced methods like GW or hybrid functional could give satisfying results.[36] We also use the hybrid functional HSE06 to verify the different magnetic configurations of the PBE results. Under the HSE06 functional, the ground state is still FM, but the energy difference between the FM and the lowest antiferromagnetic (AFM) state is 26 meV. The spin density and band structure of the FM ground state calculated with the HSE06 functional are shown in Fig. 2(b) and (f). The band structures of the AFM states are presented in Fig. S1 (ESI†). Compared with the PBE results, the HSE06 spin density decreases slowly with increasing distance away from the edges, while the total magnetic moment is still 2.00 μ_B. The H-14-2H ZGNR is still a BMS, but the band gap changes from 0.23 eV (with PBE functional) to 0.64 eV (with HSE06 functional). $\Delta 2$ and $\Delta 3$ also change to 0.28 and 0.30 eV, respectively. This is consistent with the results of Louie and Jiang *et al.* for ZGNRs.[27,36]

We also examine the effect of width and functional (PBE and HSE06) on the $\Delta 1$, $\Delta 2$, and $\Delta 3$ values, and the main results are shown in Table 1. Regardless of the width, the H-*N*-2H ZGNRs are always in BMS with FM ground state, as confirmed by HSE06 calculations. Independent of the exchange functional used (PBE or HSE06), $\Delta 1$, $\Delta 2$, and $\Delta 3$ all decrease as the width increases. In addition, we also find that $\Delta 1$ calculated by HSE06 functional is bigger than that by PBE, and $\Delta 2$, $\Delta 3$ are smaller than those calculated by PBE functional with different *N*.

Table 1 The energy gap parameters $\Delta 1$, $\Delta 2$, and $\Delta 3$ (in eV units) for the H-*N*-2H ZGNRs (*N* = 6 to 20) calculated using PBE and HSE06 functionals

	PBE			HSE06		
N	$\Delta 1$	$\Delta 2$	$\Delta 3$	$\Delta 1$	$\Delta 2$	$\Delta 3$
6	0.55	0.89	0.84	1.42	0.71	0.71
8	0.43	0.66	0.65	1.11	0.53	0.56
10	0.33	0.54	0.55	0.89	0.40	0.43
12	0.27	0.43	0.44	0.72	0.33	0.38
14	0.23	0.36	0.40	0.64	0.28	0.30
16	0.20	0.33	0.36	0.54	0.25	0.27
18	0.17	0.28	0.31	0.46	0.21	0.26
20	0.11	0.27	0.29	0.40	0.16	0.19

3.2 The electronic and magnetic properties of H-*M*-LD-*N*-2H

We have found that H-ZGNR-2H is a typical BMS. Early work demonstrated that BMS could be tuned into a half-metal by a transverse electrical field or by element doping.[11,39] Besides, it is known that a 5-8-5 line-defect is a common line defect embedded in graphene, consisting of one octagonal and two pentagonal carbon rings (Fig. 1(b)). Previous works have shown that line defects could effectively tune the electronic structures of ZGNRs by introducing defect states near the Fermi level, thus reducing the band gap.[42,43] From this point of view, we introduce the 5-8-5 line defect into the H-ZGNRs-2H, forming H-*M*-line-defect-*N*-2H ZGNRs as defined before.[42] Herein, *M* (*N*) represents the number of perfect C chains at the left (right) of the line defect. In terms of the values of *M* and *N*, the modified ZGNRs can be classified into two groups: "symmetrical" ones with $M = N$, and "unsymmetrical" ones with $M \neq N$. The structure of a "symmetrical" ribbon of H-6-LD-6-2H is shown in Fig. 1(b) as an example.

At first, we examine the energy of different magnetic configurations to determine the ground state. Fig. 3(a) and (b) show the spin density of the AFM and FM configurations of the H-6-LD-6-2H ZGNRs, and the energy of the AFM configuration is higher than that of the FM by 6 meV. So the ground state is still FM, which is similar to the case of the H-14-2H ZGNR without line defect discussed in the previous section.[29] The magnetic moments in the supercell of the AFM and FM configurations are 0.98 and 1.98 μ_B, respectively. The spin densities are mainly localized at the sp^2-edge C atoms and the next-to-edge C atoms of the sp^3 edge, also similar to the H-14-2H case shown in Fig. 2(e). For the FM ground state, the magnetic contribution from these edge C atoms is about 1.20 μ_B. The band structures of the AFM and FM configurations are also shown in Fig. 3(c) and (d), respectively. The AFM state is a metal with a Dirac point, which is similar to the case of perfect H-14-2H ZGNR.[27] The FM state shows half-metallic character: the α-spin

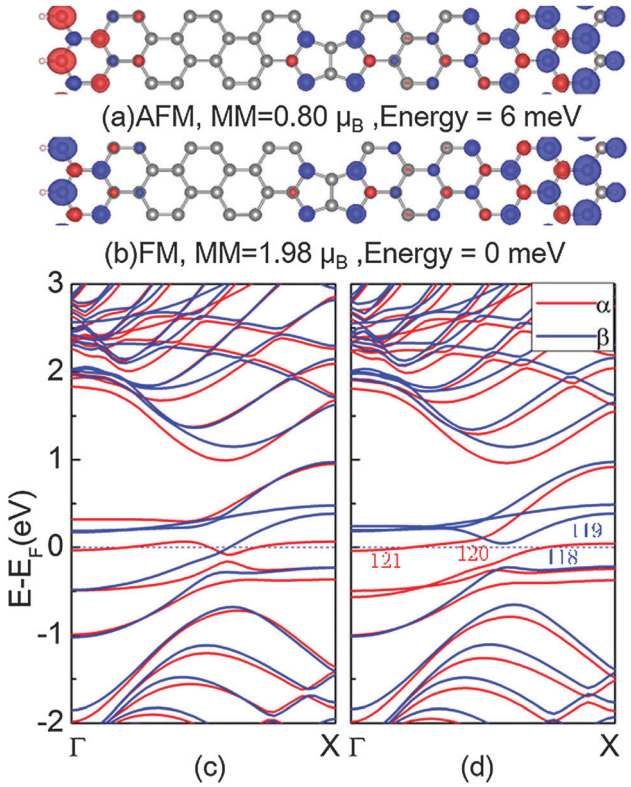

Fig. 3 The spin densities of the (a) AFM and (b) FM configurations and band structures of the (c) AFM and (d) FM of the H-6-LD-6-2H calculated by the PBE. The red circle (line) and blue circle (line) are for the α-spin and β-spin, respectively. The numbers in (d) present the I band used in supporting materials.

channel is metallic, while the β-spin channel is semiconducting with a gap of 0.27 eV. To find the spatial distribution of the states around the Fermi energy, the charge densities of these states at some special *k*-points in the first Brillouin zone are shown in Fig. S2(a–d) (ESI†). These states are mainly localized at C atoms of the edges and the line defect, which indicates the localized electron character.[40]

Again, we use the HSE06 functional to check whether H-6-LD-6-2H is really a half-metal. The band structure and partial density of states (PDOS) calculated by HSE06 are shown in Fig. 4(a) and (b). The α-spin channel is still metallic, while the β-spin channel shows semiconducting behavior with a gap of 0.56 eV, confirming that H-6-LD-6-2H is indeed a half-metal. The VBM and CBM of β-spin bands lie at the same *k*-point of $3\pi/5a$ in the first Brillouin zone. The HSE06 band gap of β-spin channel is 0.29 eV larger than the PBE value. In order to explore the origin of the half-metallicity, we calculate the PDOS of H-6-LD-6-2H, shown in Fig. 4(b). It is clear that the states near the Fermi level are mainly contributed by the C atoms of the line defect (black line), while the C atoms of the sp^3-edge (green line) show no obvious contribution to the states at the Fermi energy. The states below and above the Fermi energy by 1 eV are contributed by C atoms of the sp^2-edge (yellow line). Moreover, the H atoms also hybridize with edge C atoms, which is similar to the case of H-ZGNR-H.[2]

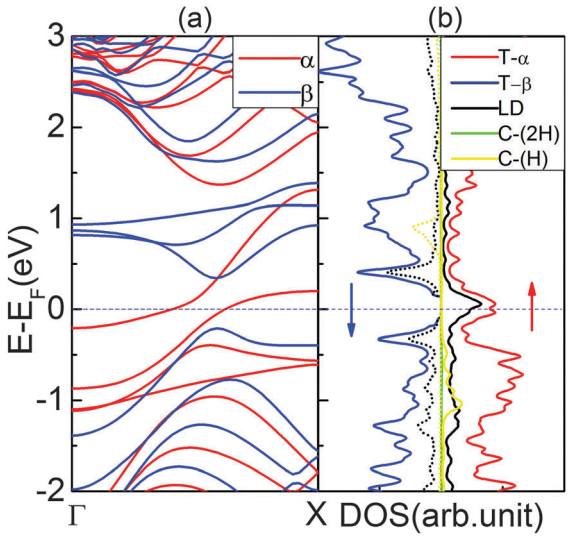

Fig. 4 (a) The band structure and (b) density of the states of the H-6-LD-6-2H, calculated by HSE06. In (a), the red and blue lines are for α-spin and β-spin, respectively. In (b), the red, black, green and yellow lines denote the total DOS and the PDOS of C atoms belonging to the line defect, of edge C atoms (sp^3), and edge C atoms (sp^2), respectively. The corresponding dashed lines present α-spin and β-spin.

When the line defect is introduced into the GNRs, the states near Fermi energy are mainly contributed by the C atoms of the line defect instead of the edge C atoms. More details are shown in Fig. S3 (ESI†). Li *et al.* found that when the line defect is embedded into the H-ZGNRs-H, resulting in an AFM semiconductor ground state, the VBM and CBM are also composed of the states of C atoms from the line defect.[42] From the viewpoint of geometry, the edges of H-6-LD-6-2H are saturated with one H atom (left side) and 2H atoms (right side), and thus the symmetry of the original H-6-LD-6-H is broken, tuning the system from antiferromagnetic semiconductor to ferromagnetic half-metal.

Similarly, we also explore the effect of the width of ribbons with the line defect. We first study the electronic properties of the "symmetrical" H-*M*-LD-*M*-2H using PBE and HSE06 functionals (the number of perfect C chains on both sides of the line defect is the same, $M = N$), as shown in Fig. 5. For $M = 4$ and 8, the band gaps given by PBE are 0.36 and 0.24 eV, while these corresponding values given by HSE06 are 0.66 and 0.38 eV, respectively. Compared with the results of PBE, HSE06 gives an obvious up-shift of the energy gaps, while this shift becomes smaller when the width increases. No matter how the width *M* changes, the H-*M*-LD-*M*-2H ZGNRs are all half-metals at the FM ground state, and the total magnetic moments equal to about 2.00 μ_B. Among the AFM configurations, the lowest energy ones are all metals with a Dirac point, with a total magnetic moment of 0.81 μ_B. As the width increases, the energy difference between the FM and AFM states monotonically decreases from 42 meV with $N = 4$ to 14 meV with $N = 8$ calculated using the HSE06 functional.

We also study the electronic and magnetic properties of the "unsymmetrical" H-*M*-LD-*N*-2H ($M \neq N$) with other *M* or *N* values.

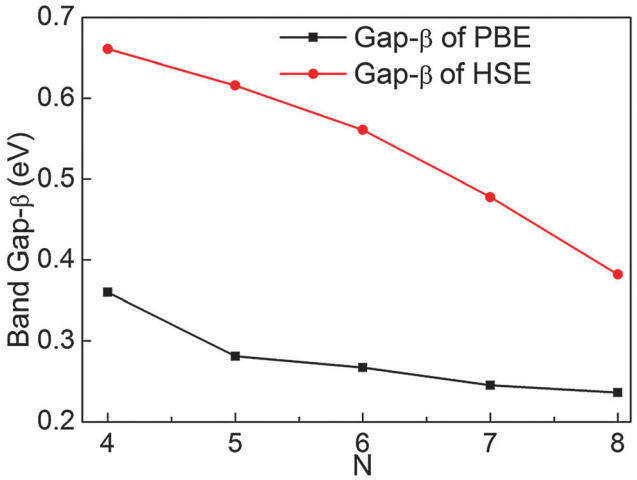

Fig. 5 The energy gap of the β-spin channel varies with the width of H-*M*-LD-*M*-2H, calculated by PBE (black line) and HSE06 (red line).

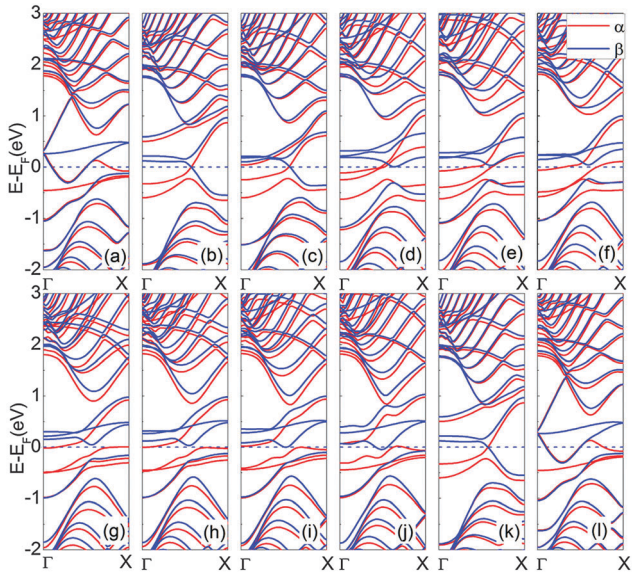

Fig. 6 The band structures of H-*M*-LD-*N*-2H for $M + N = 12$: (a) H-12-LD-0-2H, (b) H-11-LD-1-2H, (c) H-10-LD-2-2H, (d) H-9-LD-3-2H, (e) H-8-LD-4-2H, (f) H-7-LD-5-2H, (g) H-6-LD-6-2H, (h) H-5-LD-7-2H, (i) H-4-LD-8-2H, (j) H-3-LD-9-2H, (k) H-2-LD-10-2H, (l) H-1-LD-11-2H.

The band structures of the H-*M*-LD-*N*-2H ($M + N = 12$) are shown in Fig. 6. H-12-LD-0-2H [Fig. 6(a)] and H-0-LD-12-2H [Fig. 6(l)], with the line defect at the edge of the ribbons, are all spin-polarized metal, which are the same as H-0-LD-12-H and H-12-LD-0-H.[42] The shape and charge density distributions of the bands are similar to each other for these two geometries (H-0-LD-12-H and H-12-LD-0-H).[42] When the line defect is moved from the edge to the center of the ribbons, as shown in Fig. 6(b), (c), and (k), these ribbons change into a metal with a Dirac point, similar to the bands of the AFM-I configuration of the H-ZGNRs-2H in Fig. S1 (ESI†).[42] When $N = 3$ or $M = 3$, the ribbons turn from metal with a Dirac point into normal spin-polarized metal. The bands of α-spin and β-spin channels are both closed at the Fermi energy. When the line defect is moved to the center of the ribbon, as shown in Fig. 6(e–h), the α-spin channel is metallic with energy bands crossing the Fermi energy, but the β-spin channel remains semiconducting with the band gap changing from 0.29 (for e), 0.26 (for f), 0.21 (for g) to 0.16 eV (for h) (calculated by PBE). Again, we recalculate these gap values by HSE06, and the band gaps for the β-spin channel of the corresponding systems shown in Fig. 6(e–h) are 0.54, 0.54, 0.56, and 0.56 eV, respectively. So the systems shown in Fig. 6(e–h) are all still half metal, contributed by the C atoms of the line defect, similar to the PBE results. The states near the Fermi energy are still contributed by the C atoms of the line defect.

If we consider the H-ZGNR-2H as the prototype (BMS), the H-*M*-LD-*N*-2H ($M > 3$, $N > 3$) can be considered as prototypes doped with the line defect, and they now represent half-metallicity. Kang *et al.* pointed out that H-ZGNRs-2H with B or N atoms could be tuned from BMS into half-metal.[47–50] The line defect may thus be viewed as a kind of "self-doping" (without other elements doped). Varying the position of the line defect, the β-spin channel changes from a direct gap semiconductor to an indirect gap semiconductor. In a word, the H-*M*-LD-*N*-2H ZGNRs vary from the spin-polarized metal to the metal with Dirac point, as well as the half-metal, by changing the position of the line defect.

We study "unsymmetrical" H-*M*-LD-*N*-2H ($M = 6$, $N = 5$) as a reference. The calculated total magnetic moment equals 1.98 μ_B, and $\Delta E = E_{FM} - E_{AFM} = -3$ meV, suggesting a FM ground state. In sum, the line defect suppresses the effects of edge functionalization when the line defect lies at the edge, and the electronic and magnetic properties are similar to those of the H-LD-H ZGNRs.[42] Other defects such as vacancy and grain boundaries show similar effects.[44–46] When the line defects are far away from the edge, the ribbons also show half-metallicity with FM ground state.

We also calculate the H-ZGNRs-2H embedded with two line defects, and find that the system is a spin-polarized metal, as shown in Fig. S5 (ESI†). The high concentration of line defects will destroy the conjugate structure, decreasing the thermal stability of the ZGNRs. Thus, there is no need to study two or more line defects embedded in ribbons.

3.3 The stability of H-*M*-LD-*N*-2H

To examine whether H-*M*-LD-*N*-2H is stable and whether the magnetic state could survive at room temperature, we further perform *ab initio* molecular dynamics (AIMD) simulations. The simulation time of one trajectory is 10 ps. As an example, the fluctuation of temperature, total energy, and total magnetic moments of H-6-LD-6-2H are given in Fig. 7(a)–(c), respectively. The results indicate that H-6-LD-6-2H is stable at room temperature. During the simulation, the ribbon maintains the planar geometry. This can be easily understood from the fact that the binding energies of the C–H and C–C bonds are much larger than the thermal energy at room temperature. Similar results were also observed in the case of H-ZGNR-2H.[27] The total energy oscillates around −549.51 eV after 2 ps, with the amplitude being about 0.017 eV per atom.

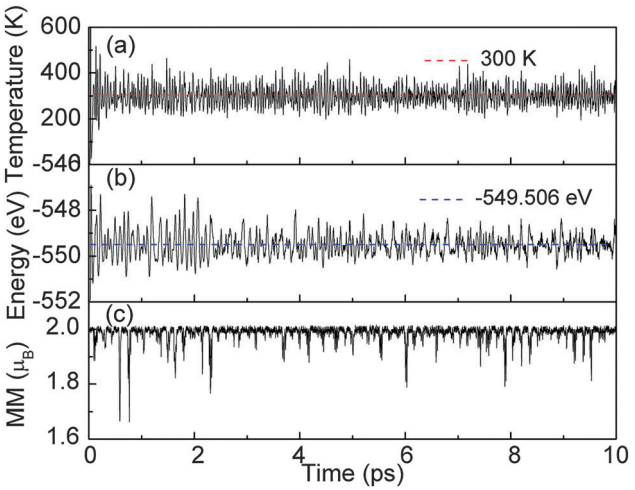

Fig. 7 (a) The temperature, (b) total energy, and (c) total magnetic moments of H-6-LD-6-2H as a function of MD simulation time at 300 K.

The total magnetic moment also oscillates around the average value of 2.0 μ_B. It is clear that the H-6-LD-6-2H is at its magnetic ground structure with the FM ground state. In addition, we also perform test calculations for several other H-*M*-LD-*N*-2H structures and get similar results.

4. Conclusions

We systematically study the electronic and magnetic properties of H-ZGNRs-2H and H-line-defect-2H ZGNRs with different widths. It is found that H-ZGNRs-2H are typical BMSs. In the H-*M*-LD-*N*-2H ZGNRs, the edges provide ferromagnetic ground states, while the line defect contributes to the states near Fermi level. The introduction of line defect can be seen as a "self-doping" mechanism without introducing foreign elements. We also reveal the effect of the location of the line defect by changing the position of the line defect, with the width of ZGNRs fixed. The H-*M*-LD-*N*-2H ZGNRs are half-metals with FM ground states when the line-defect is at least four chains away from the edge of the ZGNRs, and the same results are found with HSE06 calculations. As the line defect moves toward the edge of the ZGNRs, the systems become normal spin-polarized metals or metals with Dirac point, depending on the position of the line defect and regardless of the width of H-*M*-LD-*N*-2H. Finally, we check the structural and magnetic stability at room temperature by AIMD. Our work offers a feasible strategy to design carbon nanostructures with different properties for nanoelectronics and spintronics applications.

Acknowledgements

We thank Haifeng Sun and Qunxiang Li for useful discussions. This work was supported by the National Natural Science Foundation of China (Grant No. 11334006). C. S. acknowledges the National Natural Science Foundation of China (Grant No. 11504015). The computational resources from the SCCAS, Shanghai Supercomputer center, National Supercomputing Center in Tianjin and Guangzhou, USTC and Tsinghua Supercomputer Centers are acknowledged.

Notes and references

1 Y. W. Son, M. L. Cohen and S. G. Louie, *Nature*, 2006, **444**, 347–349.
2 Y. W. Son, M. L. Cohen and S. G. Louie, *Phys. Rev. Lett.*, 2006, **97**, 216803.
3 B. Verónica, H. Oded and E. S. Gustavo, *Nano Lett.*, 2006, **6**, 2748–2754.
4 T. H. DepositeVo, M. Shekhirev, D. A. Kunkel, M. D. Morton, E. Berglund, L. Kong, P. M. Wilson, P. A. Dowben, A. Enders and A. Sinitskii, *Nat. Commun.*, 2014, **5**, 3189–3197.
5 G. Z. Magda, X. Z. Jin, I. Hagymasi, P. Vancso, Z. Osvath, P. Nemes-Incze, H. C. Wang, L. P. Biro and L. Tapaszto, *Science*, 2014, **514**, 608–611.
6 M. Y. Han, B. Özyilmaz, Y. B. Zhang and P. Kim, *Phys. Rev. Lett.*, 2007, **98**, 206805.
7 Q. M. Yan, B. Huang, J. Yu, F. W. Zheng, J. Zang, J. Wu, B. L. Gu, F. Liu and W. H. Duan, *Nano Lett.*, 2007, **7**, 1469–1473.
8 V. M. Pereira and N. A. H. Castro, *Phys. Rev. Lett.*, 2009, **103**, 046801.
9 H. Oded, B. Verónica, J. E. Peralta and G. E. Scuseria, *Nano Lett.*, 2007, **7**, 2295–2299.
10 L. Yang and J. Guo, *Nano Res.*, 2010, **3**, 189–199.
11 E. J. Kan, Z. Li, J. L. Yang and J. G. Hou, *Appl. Phys. Lett.*, 2007, **91**, 243116.
12 Z. Y. Li, H. Y. Qian, J. Wu, B. L. Gu and W. H. Duan, *Phys. Rev. Lett.*, 2008, **100**, 206802.
13 E. J. Kan, Z. Y. Li, J. L. Yang and J. G. Hou, *J. Am. Chem. Soc.*, 2008, **130**, 4224–4225.
14 D. Jiang, B. G. Sumpter and S. J. Dai, *J. Chem. Phys.*, 2007, **126**, 134701.
15 D. W. Boukhvalov and M. I. Katsnelson, *Nano Lett.*, 2008, **8**, 4373–4379.
16 T. B. Martins, A. J. R. da. Silva, R. H. Miwa and A. Fazzio, *Nano Lett.*, 2008, **8**, 2293–2298.
17 H. Lee, Y. W. Son, N. Park, S. Han and J. Yu, *Phys. Rev. B: Condens. Matter Mater. Phys.*, 2005, **72**.
18 G. Lee and K. Cho, *Phys. Rev. B: Condens. Matter Mater. Phys.*, 2009, **79**, 165440.
19 O. V. Yazyev and L. Helm, *Phys. Rev. B: Condens. Matter Mater. Phys.*, 2007, **75**, 125408.
20 B. Huang, F. Liu, J. Wu, B. L. Gu and W. H. Duan, *Phys. Rev. B: Condens. Matter Mater. Phys.*, 2008, **77**, 153411.
21 Y. C. Chang and S. Haas, *Phys. Rev. B: Condens. Matter Mater. Phys.*, 2011, **83**, 085406.
22 S. Okada, K. Nakada, K. Kuwabara, K. Daigoku and T. Kawai, *Phys. Rev. B: Condens. Matter Mater. Phys.*, 2006, **74**, 121412.
23 L. Z. Kou, C. Tang, W. L. Guo and C. F. Cheng, *ACS Nano*, 2011, **5**, 1012–1017.
24 G. P. Tang, Z. H. Zhang, X. Q. Deng, Z. Q. Fan and H. L. Zhu, *Phys. Chem. Chem. Phys.*, 2015, **17**, 638–643.

25 N. Ansari, F. Nazari and F. lllas, *Phys. Chem. Chem. Phys.*, 2014, **16**, 21473–21485.
26 G. P. Tang, J. C. Zhou, Z. H. Zhang, X. Q. Deng and Z. Q. Fan, *Carbon*, 2013, **60**, 94–101.
27 B. Xu, J. Yin, Y. D. Xia, X. G. Wan, K. Jiang and Z. G. Liu, *Appl. Phys. Lett.*, 2010, **96**, 163102.
28 G. Kresse and J. Furthmüller, *Comput. Mater. Sci.*, 1996, **6**, 15–50.
29 G. Kresse and J. Furthmüller, *Phys. Rev. B: Condens. Matter Mater. Phys.*, 1996, **54**, 11169–11186.
30 P. E. Blochl, *Phys. Rev. B: Condens. Matter Mater. Phys.*, 1994, **50**, 17953–17979.
31 G. Kresse and D. Joubert, *Phys. Rev. B: Condens. Matter Mater. Phys.*, 1999, **59**, 1758–1775.
32 J. P. Perdew, K. Burke and M. Ernzerhof, *Phys. Rev. Lett.*, 1996, **77**, 3865–3868.
33 J. Heyd, G. E. Scuseria and M. Ernzerhof, *J. Chem. Phys.*, 2006, **124**, 219906.
34 S. Nosé, *Mol. Phys.*, 1984, **52**, 255–268.
35 G. J. Martyna, M. L. Klein and T. Mark, *J. Chem. Phys.*, 1992, **97**, 2635–2643.
36 Y. Li, C. H. Park, Y. W. Son, M. L. Cohen and S. G. Louie, *Phys. Rev. Lett.*, 2007, **99**, 186801.
37 X. X. Li, X. J. Wu, Z. Y. Li, J. L. Yang and J. G. Hou, *Nanoscale*, 2012, **4**, 5680–5685.
38 X. X. Li and J. L. Yang, *Phys. Chem. Chem. Phys.*, 2013, **15**, 15793–15801.
39 L. Yuan, Z. Y. Li and J. L. Yang, *Phys. Chem. Chem. Phys.*, 2013, **15**, 497–503.
40 T. Miyake and S. Satio, *Phys. Rev. B: Condens. Matter Mater. Phys.*, 2003, **68**, 155424.
41 X. X. Li, X. J. Wu and J. L. Yang, *J. Mater. Chem. C*, 2013, **1**, 7197–7201.
42 Z. Y. Guan, Q. X. Li and X. J. Wu, *Nano LIFE*, 2012, **2**, 124003.
43 J. Lahiri, Y. Lin, P. Bozkurt, I. I. Oleynik and M. Batzill, *Nat. Nanotechnol.*, 2010, **5**, 326–329.
44 Z. Y. Guan, W. Y. Wang, J. Huang, X. J. Wu, Q. X. Li and J. L. Yang, *J. Phys. Chem. C*, 2014, **118**, 28616–28624.
45 J. Coraux, A. T. N. Diaye, C. Busse and T. Michely, *Nano Lett.*, 2008, **8**, 565–570.
46 J. Cervenka, M. I. Katsnelson and C. F. J. Flipse, *Nat. Phys.*, 2009, **5**, 840–844.
47 J. Kang, F. M. Wu and J. B. Li, *Appl. Phys. Lett.*, 2011, **98**, 083109.
48 L. H. Wang, Z. Z. Zhang, J. G. Zhao, B. J. Ding and Y. Guo, *J. Electron Microsc.*, 2015, **11**, 1–10.
49 D. Zhang, M. Q. Long, X. J. Zhang, F. P. Ouyang, M. J. Li and H. Xu, *Appl. Phys. Lett.*, 2015, **117**, 014311.
50 X. F. Yang, W. Q. Zhou, X. K. Hong, Y. S. Liu, X. F. Wang and J. F. Feng, *J. Chem. Phys.*, 2015, **142**, 024706.

